Research Article Vol. 56, No. 12 / April 20 2017 / *Applied Optics* 3281

applied optics

Precise calibration of pupil images in pyramid wavefront sensor

YONG LIU,[1,2] QUANQUAN MU,[1,*] ZHAOLIANG CAO,[1] LIFA HU,[1] CHENGLIANG YANG,[1] AND LI XUAN[1]

[1]*State Key Laboratory of Applied Optics, Changchun Institute of Optics, Fine Mechanics and Physics, Chinese Academy of Sciences, Changchun 130033, China*
[2]*University of Chinese Academy of Sciences, Beijing 100039, China*
**Corresponding author: muquanquan@ciomp.ac.cn*

Received 6 January 2017; revised 18 March 2017; accepted 21 March 2017; posted 22 March 2017 (Doc. ID 284268); published 13 April 2017

The pyramid wavefront sensor (PWFS) is a novel wavefront sensor with several inspiring advantages compared with Shack–Hartmann wavefront sensors. The PWFS uses four pupil images to calculate the local tilt of the incoming wavefront. Pupil images are conjugated with a telescope pupil so that each pixel in the pupil image is diffraction-limited by the telescope pupil diameter, thus the sensing error of the PWFS is much lower than that of the Shack–Hartmann sensor and is related to the extraction and alignment accuracy of pupil images. However, precise extraction of these images is difficult to conduct in practice. Aiming at improving the sensing accuracy, we analyzed the physical model of calibration of a PWFS and put forward an extraction algorithm. The process was verified via a closed-loop correction experiment. The results showed that the sensing accuracy of the PWFS increased after applying the calibration and extraction method.

OCIS codes: (010.1080) Active or adaptive optics; (010.7350) Wave-front sensing; (230.6120) Spatial light modulators.

https://doi.org/10.1364/AO.56.003281

1. INTRODUCTION

Adaptive optics systems (AOSs) are now widely used and necessary when observing dim targets [1–3]. An AOS uses a wavefront sensor to measure turbulence, and the most-applied wavefront sensor is a Shack–Hartmann sensor. Shack–Hartmann sensors use a microlens array to divide the whole wavefront into hundreds of subapertures, thus spot images are diffraction-limited by microlens size, which is of a 10 μm degree. This results in estimation error due to low subaperture energy. Thus, the sensing signal of a Shack–Hartmann sensor is of limited signal-to noise ratio (SNR), especially on dim targets, which are hotspots in astronomical research. To avoid the limit by the pupil size of the sensor element, the pyramid wavefront sensor (PWFS) was proposed [4]. The PWFS sensing signal is produced from system pupil images. Each pixel of these images is diffraction-limited by the pupil size of the system, which is significantly larger than that of the lenslets in the Shack–Hartmann sensor. Thus, the theoretical SNR of a PWFS signal is relatively higher than that of a Shack–Hartmann sensor [5,6]. Meanwhile, the PWFS shows various advantages such as high sensing accuracy on dim targets, adjustable sensitivity, and a large field of view [7–9]. PWFSs are currently used in many systems of the European Southern Observatory (ESO), including the Telescopio Nazionale Galileo and Large Binocular Telescope, and the infrared system in the Calar Alto Observatory. The on-sky test showed that systems using the PWFS achieved great performance in closed-loop correction of real turbulence [10,11].

A PWFS consists of a focus lens, a pyramid prism, a relay lens, and a CCD camera. Thus, calibration of the system involves relationships among these elements, and affects the intensity distribution and positions of pupil images on the CCD plane. Theoretically, pupil images are supposed to be fixed, but in practice due to the noise and turbulence, the edges and their sizes would be hard to determine, and the diffraction halo would make the images blur. Mispositioning of these images would produce a low-order but relatively large error in the reconstructed wavefront. In a closed-loop case, this noise is considered as the initial system error and can be compensated for along the iteration. However, in AOS, using a liquid crystal spatial light modulator (LC-SLM) as the wavefront corrector, the system has to work in an open-loop mode to increase the sensing energy [12–14], and the initial error would be involved in each correction iteration afterwards. Moreover, due to the high resolution of LC-SLM, AOS with an LC-SLM requires alignment of pixel size degree between the wavefront sensor and active area of the LC-SLM. Thus, precise extraction is of great importance in an LC-SLM-adaptive optics system. The currently used method by ESO is based on threshold binarization [15]; this method is proved to be of lower accuracy than the extraction method introduced in this paper and a comparison is shown in Section 4.

We analyzed the influence of calibration on pupil images and built a pupil extraction algorithm. Then the analytical model was verified via experiments. The results showed that fine calibration and extraction brought improvement in PWFS sensing accuracy, reducing the residual error by about 15%, and decreasing the iteration number needed to compensate for the wavefront aberration to a root-mean-square (RMS) value under $\lambda/14$.

2. FUNDAMENTALS OF PWFS

A PWFS uses a focus lens L_1 to converge the incoming wavefront onto the pyramid vertex, which is placed exactly on the focal plane. Afterwards, it will produce four outgoing rays due to the refraction of four facets of the pyramid simultaneously. These rays are converged onto the CCD camera by image lens L_2, forming four pupil images. The layout is shown in Fig. 1.

According to the existence of modulation of the spot on the pyramid vertex, PWFS can be divided into PWFS with and without modulation [16,17]. An unmodulated PWFS does not include any movable elements, so the system is stable and easy to control; however, the dynamic range is small, and thus an unmodulated PWFS cannot meet the requirement of open-loop sensing. The typical modulated PWFS applies a tip-tilt mirror (TTM) at the pupil plane to modulate the position of the focus spot on the pyramid vertex in a determined path. The modulation extends the spot to a ring to increase the dynamic range. For a PWFS with a circular modulation of 1 mrad amplitude and a pupil size of 6.4 mm, the maximum local tilt within the dynamic range is about 13λ, according to geometrical optics. This means that the modulated PWFS can cover the P-V value of real turbulence of about 12λ. Nonetheless, the relative change of sensing signals caused by turbulence decreases as the modulation averaging the incoming energy on the vertex, resulting in a low sensitivity; it also requires a long exposure time, which slows down the sensor.

By geometrically tracing the ray, for a PWFS with modulation

$$\frac{\partial W(x,y)}{\partial x} \approx \frac{\pi}{2}\frac{R}{f} S_x(x,y), \tag{1}$$

$$\frac{\partial W(x,y)}{\partial y} \approx \frac{\pi}{2}\frac{R}{f} S_y(x,y), \tag{2}$$

$W(x,y)$ is the incoming wavefront, R is the angular amplitude of modulation, f is the focal length of the focus lens, x and y are normalized coordinates on pupil. $S_x(x,y)$ and $S_y(x,y)$ are sensing signals on the x and y directions, respectively, which can be calculated as

$$S_x(x,y) = \frac{I_1(x,y) + I_4(x,y) - I_2(x,y) - I_3(x,y)}{\sum_i I_i(x,y)}, \tag{3}$$

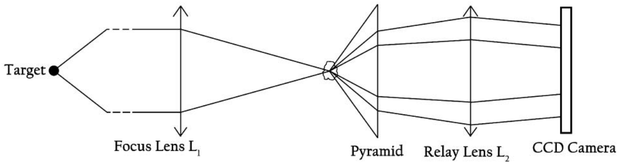

Fig. 1. Optical layout of PWFS.

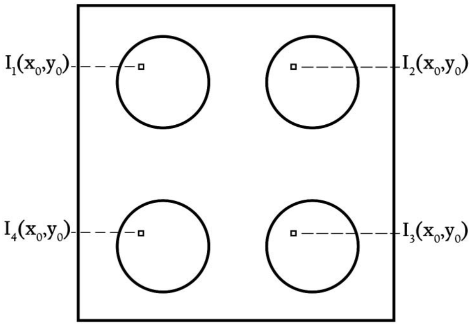

Fig. 2. Sketch of pupil images on CCD camera.

$$S_y(x,y) = \frac{I_1(x,y) + I_2(x,y) - I_3(x,y) - I_4(x,y)}{\sum_i I_i(x,y)}. \tag{4}$$

The sketch of pupil images is shown in Fig. 2.

We can conclude from Eqs. (1)–(4) that the accuracy of sensing signals is important in reconstruction. However, due to the interference between adjacent images, the diffraction of the pyramid edge, and the irregular shape of each image, the exact extraction of pupil images is hard to conduct precisely. The interferences between images are affected by the intervals between them, which could be controlled by the relative positions of the optics elements. Thus the calibration of PWFS elements was studied, and a precise extraction process was designed.

3. CALIBRATION OF OPTICAL ELEMENTS IN PWFS

Before extracting and calculating the sensing signal, calibration of the PWFS system must be done. The calibration of the optical elements in a PWFS involves calibration of the intervals between focus lens L_1, the pyramid, relay lens L_2, and the CCD camera, and adjusting the six-dimensional altitudes of the pyramid: three-dimensional translations and three-dimensional rotations [18]. After calibration, pupil images on the CCD were equally distributed, and the conjugation relation was guaranteed so that when the tilt modulation was added, all pupil images stayed in the same positions. This process removes the static aberration induced by the misalignment of the pyramid and ensures that the pupil image positions were fixed for the extraction. Without this calibration, the extraction would have to be conducted constantly to catch up with the modulation, which was unrealistic for the sensor.

4. HIGH-PRECISION EXTRACTION OF PUPIL IMAGES

Pupil images are supposed to be four perfect circles according to the design, and need to be extracted from the CCD frame to speed up the calculation. The principle of a PWFS requires a highly corresponding relation among every extracted image. If the center position were misaligned, a high-order and tilt error would be introduced. Figure 3 shows the error produced by a shift of 1 pixel in the x direction for each pupil image; the initial wavefront was a random turbulence with a RMS value of 0.152 μm.

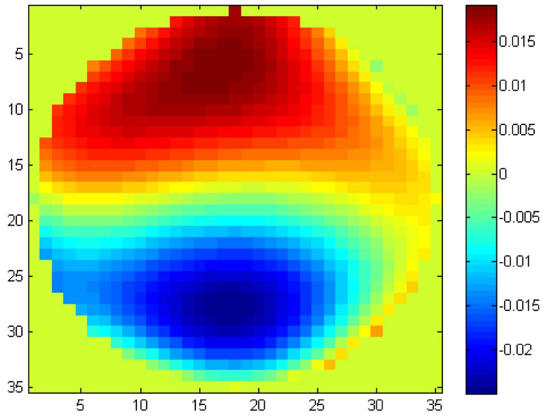

Fig. 3. Error introduced by shifting each pupil image by 1 pixel in the x direction; RMS value was 0.015 μm, initial wavefront was a random turbulence with RMS value of 0.089 μm.

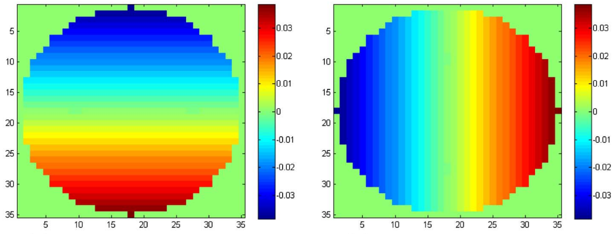

(a) S_x of first-order defocus (b) S_y of first-order defocus

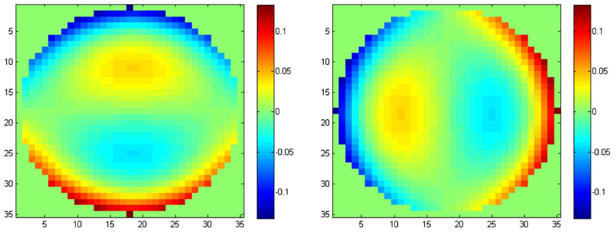

(c) S_x of second-order defocus (d) S_y of second-order defocus

Fig. 4. S_x and S_y of first-order and second-order defocus.

Basically, the extraction process of pupil images is based on threshold extraction. First, a background threshold is determined after removing the average noise and background grayscale value of the image. Then, all the points that have a value lower than the threshold are set to zero, and all the nonzero points are extracted as the sensing signal to calculation.

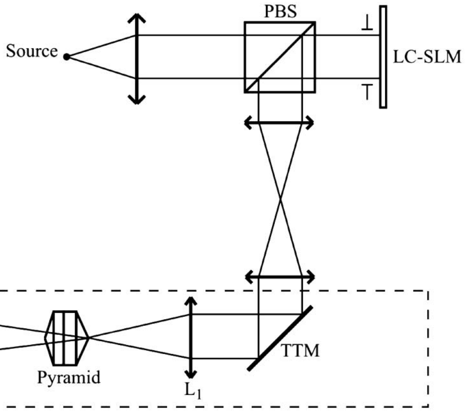

Fig. 6. Optical layout of PWFS-LC-SLM closed-loop correction.

However, in practical conditions, due to the blur of the image edge, the threshold extraction usually gets pupils larger than the real ones. Moreover, the random CCD noise and interference would stretch the edges of the pupil images and shake the image centers, resulting in location error. Thus, a high-precision extraction process is designed.

Correlation is used in the image processing algorithm to match the subregion of the sample image with a specific mask. In MATLAB, we can compute the correlation coefficient between two matrices of the same size. The correlation of two matrices is defined as

$$r = \frac{\sum_m \sum_n (A_{mn} - \bar{A})(B_{mn} - \bar{B})}{\sqrt{\left(\sum\limits_m \sum\limits_n (A_{mn} - \bar{A})^2\right)\left(\sum\limits_m \sum\limits_n (B_{mn} - \bar{B})^2\right)}}. \tag{5}$$

This inspires us to calculate the correlation of sensing signals of a circularly symmetric wavefront to align the pupil images. The sensing signals in the x and y directions coming out of a PWFS are proportional to the gradients of the incoming wavefront according to Eqs. (3) and (4). For a circularly symmetric wavefront—for example, the defocus—the signals are two identical matrices after rotating one 90 degrees, as shown in Fig. 4. Thus their correlation is 1. To reduce the impact from noises

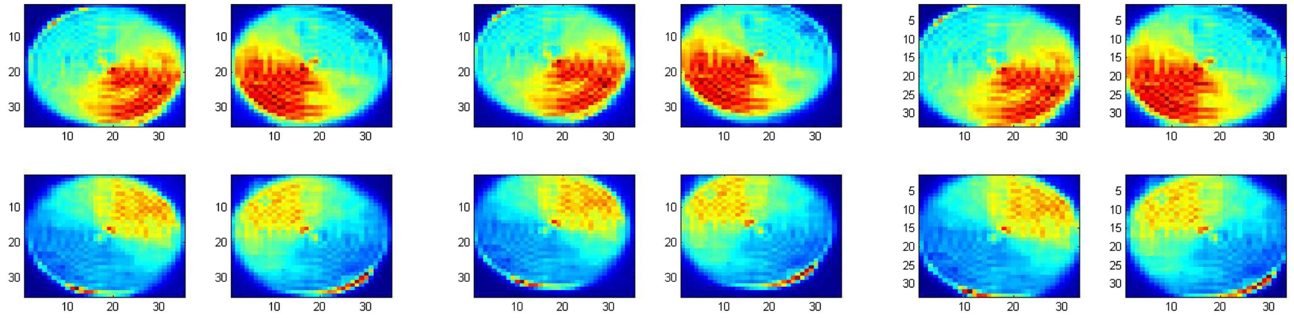

(a) signal before shaken (b) signal after shaken (c) signal after cutting the edge

Fig. 5. Sensing signal extracted before and after shaking the center. The frame could be cut smaller after the shake and halos were removed.

introduced before, we can add a special pattern to the signal, like a high-order wrinkle, to specialize the mask, increasing characteristic conditions in image matching. In our case, we used the high-resolution LC-SLM to create the wrinkle.

We sent a concentric circle signal to the LC-SLM, which was a very high-order defocus that cannot be seen by the system. The subframes would appear to have the same pattern as the concentric circles. We shook the center of each pupil image by changing its coordinate (x_n, y_n) to that of all eight adjacent points, such as $(x_n \pm 1, y_n \pm 1)$, $(x_n \pm 1, y_n)$, and $(x_n, y_n \pm 1)$ in the extraction algorithm, getting nine images of each subframe with different centers and $9^4 = 6561$ sets of all four pupil images in total. The correlation of the S_x and S_y from Eqs. (3) and (4) were calculated for all 6561 sets. The correlation value would be exactly 1 if the centers of all concentric frames in one set coincided, but due to the random noise and static aberration, the value could not reach the theoretical expectation; we could only choose the set with the highest correlation as the final signal frame.

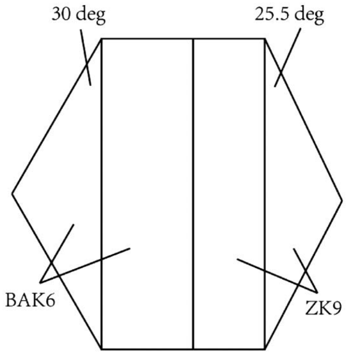

Fig. 7. The double-pyramid scheme; the front pyramid has a vertex angle of 30 deg, while the back one has 25.5 deg.

The threshold method is based on determining the full width at half maximum (FWHM) value of the pupil images. But as stated above, the pupil images edges are blurred by interference and the true size of the pupil is hard to determine; the half maximum value floats among 3–5 pixels for a pupil image of 35 pixels in diameter. The precise pupil extraction method provides the pupil center coordinate by shifting the coordinate pixel by pixel, so the accuracy of this algorithm is of pixel order.

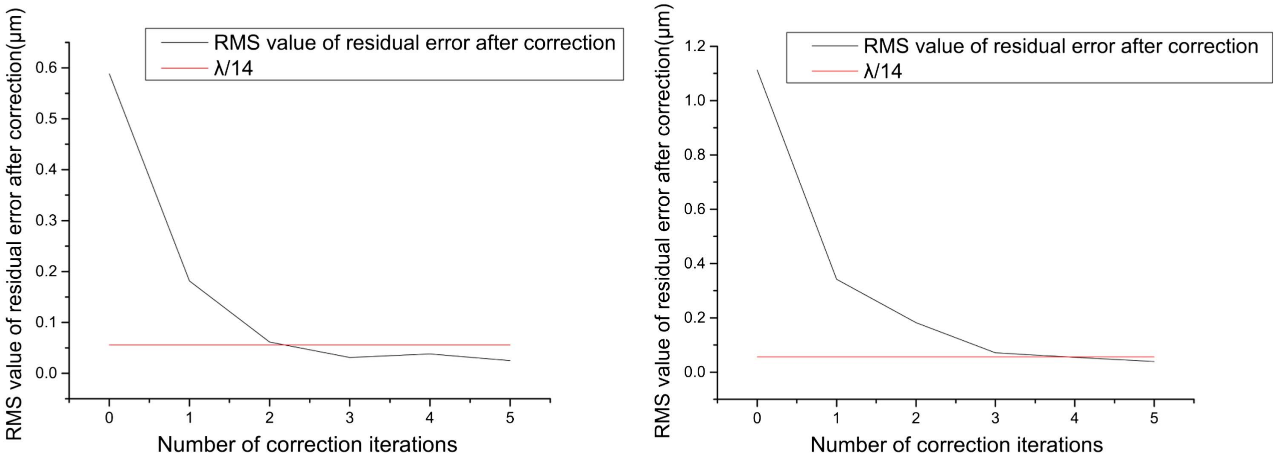

(a) initial RMS=λ

(b) initial RMS=2λ

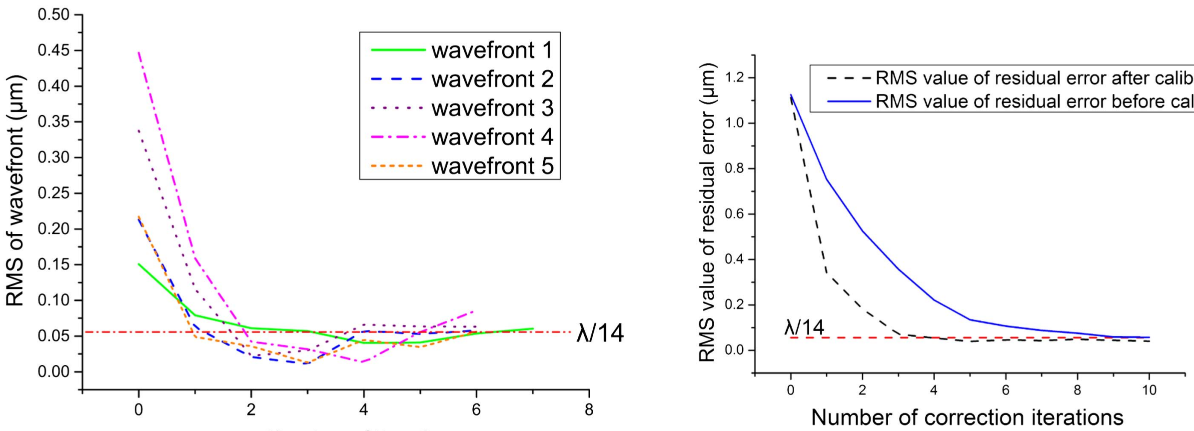

(c) correction of 5 random wavefronts

(d) comparison of residual error before and after calibration

Fig. 8. Results of closed-loop correction.

The fine extraction results are shown in Fig. 5. We could conclude from the result that the frame size needed to include all and only necessary information for reconstruction could be reduced from 35 × 35 to 33 × 33, which was closer to the theory and cut off the interference halo. The correlation value was 0.8775 for the final frame. After cutting the frame to 33 × 33, the correlation value raised to 0.9436.

5. OPTICAL DESIGN OF TEST BENCH

To verify the calibration and extraction algorithm, we designed a test bench using an LC-SLM and PWFS. In order to meet the dynamic range of real turbulence, we chose a modulated PWFS. The optical layout is shown on Fig. 6, where L1 is the focus lens and L2 is the relay lens.

A LC-SLM was used in the system to generate random turbulence according to the Kolmogorov turbulence model [19,20]. The turbulence was generated as a weighting summation of the first 16 Zernike polynomials, with coefficients produced randomly following the turbulence model. The LC-SLM also worked as the wavefront corrector in the experiment. The PWFS would send the reconstructed wavefront signal to the LC-SLM, and by subtracting the signal from the mode sent to the LC-SLM, we realized a closed-loop correction process with the least elements.

A TTM was used to produce the modulation. The dynamic range of the TTM was 1 mrad, so the modulation amplitude was set to ±0.5 mrad, expanding the PWFS dynamic range to $\approx 13\lambda$.

We used a double pyramid to replace the single-pyramid scheme. Its equivalent vertex angle equals to the difference between the front and back pyramid vertex angle multiplied with their refractive indices, respectively [21,22]. As shown in Fig. 7, the equivalent angle of this pyramid is

$$\alpha = 30^\circ \times (n_{\mathrm{BAK6}} - 1) - 25.5^\circ \times (n_{\mathrm{ZK9}} - 1) = 1.094^\circ. \qquad (6)$$

This design granted better edges and simpler fabrication of the pyramids. And by choosing proper glass, the chromatic aberration was reduced.

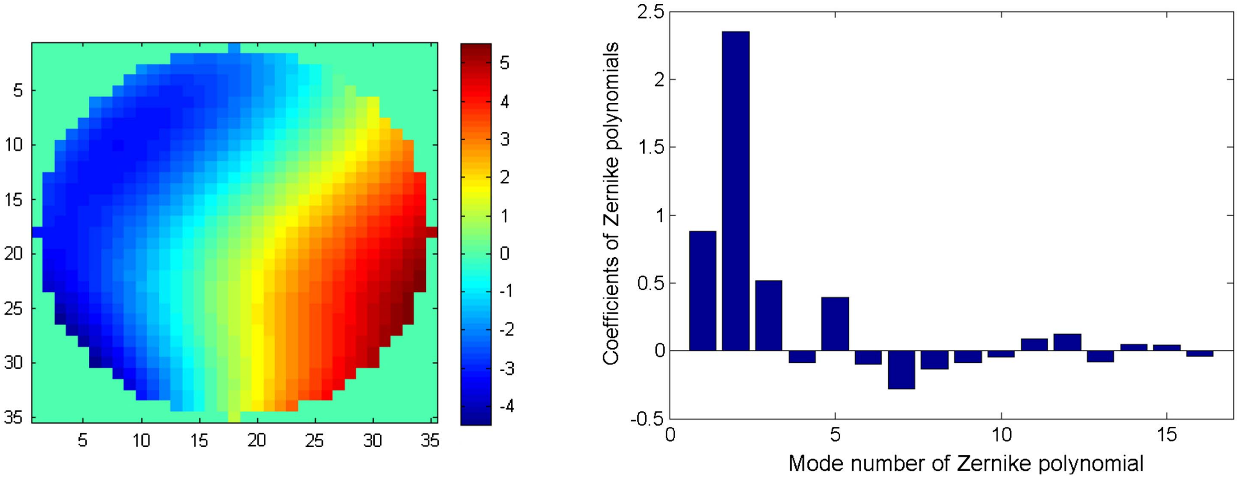

(a) a random turbulence with RMS=0.6548 μm

(b) coefficients of the turbulence in (a)

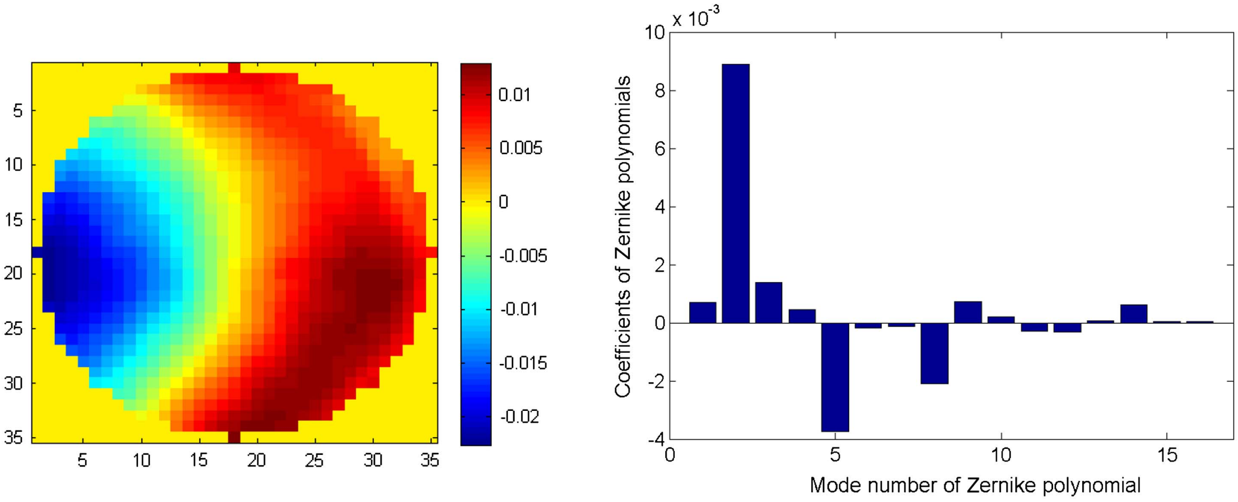

(c) wavefront after correction

(d) coefficients after correction

Fig. 9. Results of correction of a random turbulence after calibration.

6. CLOSED-LOOP CORRECTION BY LC-SLM-PWFS SYSTEM

After the calibration, using an LC-SLM as the wavefront corrector and a PWFS the sensor, we conducted correction of random static aberrations in a closed-loop system. The turbulence wavefront was produced with the first 16 terms of the Zernike polynomial, based on the Kolmogorov turbulence theory, the RMS values of the turbulence were λ and 2λ. The results of the correction are shown in Figs. 8 and 9.

As can be shown in the results, the turbulence was corrected to a RMS value less than $\lambda/14$ in 3–4 iterations, meaning the system nearly reached the diffractive limit. This shows that the steady-state error reached the requirement of adaptive correction. And the comparison of residual error before and after fine calibration reveals an improvement in the sensing accuracy and the system's convergence speed. However, the residual error of the first iteration could not meet the requirement of open-loop correction. We supposed that this may be because the pupil size coupling between the LC-SLM and PWFS was not properly ensured, inducing extra residual error.

The disadvantages of the current setup of a LC-SLM-PWFS system exist in the pupil coupling between the PWFS and LC-SLM and the precise measurement of the interaction matrix, while the extraction of pupil images based on the threshold method is not accurate enough, inducing a fake high-order signal in the sensor. By improving the extraction algorithm and precisely measuring the interaction matrix, we can step further toward the goal of realizing open-loop correction based on a PWFS with LC-SLM.

7. CONCLUSION

As concluded from the closed-loop correction results, after the fine calibration, the LC-SLM-PWFS system was able to correct static turbulence and the RMS value of residual error was under $\lambda/14$ after 3–4 iterations, while the uncalibrated system needed more than 10 iterations to achieve the same goal dealing with the turbulences of a RMS value similar to ours. The response time of our LC-SLM is 0.8 ms according to the producer, and this means that the time-saving benefit from the fine calibration is about 4–5 ms in the correction process.

Also, the residual error of the system was lower than that of the uncalibrated system [23]. The result proved that the sensing accuracy was improved greatly after fine calibration, but could not yet meet the requirements of open-loop correction.

Funding. National Natural Science Foundation of China (NSFC) (11174274, 11174279).

REFERENCES

1. M. J. Booth, "Adaptive optical microscopy: the ongoing quest for a perfect image," Light: Sci. Appl. **3**, e165 (2014).
2. B. G. Jiang, Z. L. Cao, Q. Q. Mu, L. F. Hu, C. Li, and L. Xuan, "Simulated human eye retina adaptive optics imaging system based on a liquid crystal on silicon device," Chin. Phys. B **17**, 4529–4532 (2008).
3. L. Xuan, D. Y. Li, and Y. G. Liu, "Prospect of liquid crystal adaptive optics in astronomy application," Chin. J. Liq. Cryst. Disp. **30**, 1–9 (2015).
4. R. Ragazzoni, "Pupil plane wavefront sensing with an oscillating prism," J. Mod. Opt. **43**, 289–293 (1996).
5. S. Esposito and A. Riccardi, "Pyramid wavefront sensor behavior in partial correction adaptive optic systems," Astron. Astrophys. **369**, L9–L12 (2001).
6. C. Vérinaud, "On the nature of the measurements provided by a pyramid wave-front sensor," Opt. Commun. **233**, 27–38 (2004).
7. R. Ragazzoni and J. Farinato, "Sensitivity of a pyramidic wave front sensor in closed loop adaptive optics," Astron. Astrophys. **350**, L23–L26 (1999).
8. S. Esposito, A. Riccardi, and O. Feeney, "Closed-loop performance of pyramid wavefront sensor," Proc. SPIE **4034**, 184–189 (2000).
9. A. Riccardi, N. Bindi, R. Ragazzoni, S. Esposito, and P. Stefanini, "Laboratory characterization of a Foucault-like wavefront sensor for adaptive optics," in *SPIE Conference on Adaptive Optical System Technologies* (International Society for Optics and Photonics, 1998), pp. 941–951.
10. R. Ragazzoni, A. Ghedina, A. Baruffolo, E. Marchetti, J. Farinato, T. Niero, G. Crimi, and M. Ghigo, "Testing the pyramid wavefront sensor on the sky," Proc. SPIE **4007**, 423–430 (2000).
11. S. Esposito, O. Feeney, and A. Riccardi, "Laboratory test of a pyramid wavefront sensor," Proc. SPIE **4007**, 416–422 (2000).
12. L. F. Hu, L. Xuan, Y. J. Liu, Z. L. Cao, D. Y. Li, and Q. Q. Mu, "Phase-only liquid-crystal spatial light modulator for wave-front correction with high precision," Opt. Express **12**, 6403–6409 (2004).
13. Q. Mu, Z. Cao, L. Hu, D. Li, and L. Xuan, "An adaptive optics imaging system based on a high-resolution liquid crystal on silicon device," Opt. Express **14**, 8013–8018 (2006).
14. Q. Q. Mu, Z. L. Cao, D. Y. Li, L. F. Hu, and L. Xuan, "Liquid crystal based adaptive optics system to compensate both low and high order aberrations in a model eye," Opt. Express **15**, 1946–1953 (2007).
15. E. Pinna, "Study and characterization of the pyramid wavefront sensor for co-phasing," Master's thesis (Universita Degli Studi di Firenze, 2014).
16. J. B. Costa, M. Stumpf, and M. Feldt, "Testing a non-modulated pyramid wavefront sensor," Proc. SPIE **5490**, 1304–1314 (2004).
17. J. B. Costa, R. Ragazzoni, A. Ghedina, M. Carbillet, C. Verinaud, M. Feldt, S. Esposito, E. Puga, and J. Farinato, "Is there need of any modulation in the pyramid wavefront sensor?" Proc. SPIE **4839**, 288–298 (2003).
18. Y. Liu, Q. Q. Mu, Z. L. Cao, L. F. Hu, and L. Xuan, "Fine calibration of pyramid wavefront sensor," Proc. SPIE **9796**, 979602 (2016).
19. C. Liu, Q. Q. Mu, L. F. Hu, Z. L. Cao, and L. Xuan, "High precision Zernike modal gray map reconstruction for liquid crystal corrector," Chin. Phys. B **19**, 064214 (2010).
20. Z. C. Zhang, Z. You, and D. P. Chu, "Fundamentals of phase-only liquid crystal on silicon (LCOS) devices," Light: Sci. Appl. **3**, e213 (2014).
21. S. Q. Wang, C. H. Rao, H. Xian, J. L. Zhang, J. X. Wang, and Z. Liu, "Laboratory demonstrations on a pyramid wavefront sensor without modulation for closed-loop adaptive optics system," Opt. Express **19**, 8135–8150 (2011).
22. R. Ragazzoni, E. Diolaiti, and E. Vernet, "A pyramid wavefront sensor with no dynamic modulation," Opt. Commun. **208**, 51–60 (2002).
23. J. Wang, F. Bai, Y. Ning, L. Huang, and S. Wang, "Comparison between non-modulation four-sided and two-sided pyramid wavefront sensor," Opt. Express **18**, 27534–27549 (2010).